Phase and amplitude instabilities for Bénard-Marangoni convection in fluid layers with large aspect ratio

Michael Bestehorn

Institut für Theoretische Physik und Synergetik, Universität Stuttgart, Pfaffenwaldring 57/4, 70550 Stuttgart, Germany

Pattern formation in fluids heated from below is examined in the presence of a free flat surface. On that surface, the Marangoni effect is taken into account as a second instability mechanism. It is shown that phase instabilities already known from Rayleigh-Bénard convection confine the region of stable hexagons and shrink the band of stable wavelengths considerably. The problem is attacked from two sides: amplitude equations are derived explicitly from the basic hydrodynamic equations and are analyzed with regard to secondary instabilities. This results in stability diagrams analogous to earlier calculations obtained for parallel rolls in simple Rayleigh-Bénard convection. On the other hand, we developed a numerical scheme that allows for a direct integration of the fully-three-dimensional hydrodynamic equations. This method is described in detail and time series for pattern evolution are presented, showing phase and amplitude instabilities as expected from the formalism of amplitude equations. Finally we show the connection between amplitude equations and two-dimensional generalized Ginzburg-Landau equations. These models may reproduce pattern formation near convective threshold in a quantitative way. They have the advantage of being more general than the basic equations and they can be treated numerically in a much easier way. This allows the computation of pattern evolution in very-large-aspect-ratio systems.

I. INTRODUCTION

Spatial and temporal pattern formation in the field of hydrodynamic instabilities has attracted great experimental and theoretical interest since the experimental work of Bénard [1] on thermal convection in fluids at the beginning of the century (for a review see, e.g., [2–5] and references therein). Most of the experimental and theoretical research is done for fluid vessels with a closed upper surface. A uniform vertical temperature gradient is applied on a fluid located between two horizontal plates, usually good thermal conductors, as copper or sapphire. The external heating, which drives the system away from thermal equilibrium, induces an unstable density distribution of the fluid. At a certain critical temperature gradient, convection sets in, in various forms of ordered regular patterns. In this simple case, pattern formation is controlled only by the temperature gradient [6].

In the case of Bénard-Marangoni (BM) convection, a second instability mechanism occurs [7]. The fluid has an open upper surface and is in contact with the ambient air. The temperature dependence of the surface tension on that free surface can destabilize the motionless fluid state, the liquid starts to move and one very often obtains regular hexagonal fluid cells with diameter of about the same size as the depth of the fluid layer [8–10] (see Fig. 1). First quantitatively evaluated experiments were performed by Koschmieder [11].

Actually, the patterns first reported by Bénard were caused by this so-called Marangoni effect. Surface-driven convection gained again actuality due to the possibility of doing microgravity experiments in space. Without buoyancy forces, the only possible mechanism for the destabil-

ization of a pure fluid layer caused by an externally applied temperature gradient remains the Marangoni effect.

The purpose of this paper is to compute spatial and temporal evolution of patterns in BM convection and to explore the region of stability of hexagons and rolls with respect to spatially homogeneous amplitude instabilities
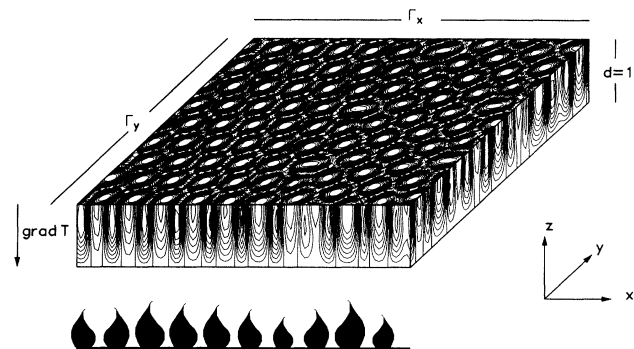

FIG. 1. The Bénard-Marangoni instability. A fluid in a rectangular container having the side lengths Γ_x, Γ_y, 1 with a free upper surface is heated from below. The motionless heat conducting state becomes unstable at a certain temperature gradient due to buoyancy effects and a temperature-dependent surface tension. A quite regular pattern of fluid motion occurs, usually in form of hexagonal patterns. In the center of each hexagon the fluid rises to the top and goes down on the side walls. The figure shows a stable state found by numerical integration of the 3D Navier-Stokes and temperature equations (see Sec. IV). The initial pattern was a randomly distributed temperature field. The vertical scale of the picture is increased by a factor of 7.5.

as well as spatially nonuniform phase instabilities. We approach this goal on three ways: (i) Investigation of amplitude equations for perfect patterns (see, e.g., [12,13]), (ii) direct numerical integration of the basic hydrodynamic equations, (iii) derivation and integration of two-dimensional (2D) models, describing three-dimensional (3D) convection [5,14–17].

For the case of convection between two rigid plates, secondary instabilities that restrict the stability region of rolls are well known since the work of Busse as the cross-roll instability and the zigzag or Eckhaus instability [18]. In the case of BM convection, we get additional instabilities: the transition from rolls to hexagons and vice versa as amplitude instabilities as well as sideband instabilities for hexagons. The latter restrict the variation of the size of stable hexagons drastically to a small band close to the critical wavelength. Recent experiments by Koschmieder and Switzer [19] on wavelength selection in BM convection confirm our computations quite well. Spatially uniform amplitude instabilities for non-Boussinesq fluids were calculated earlier, for genera systems in [20], for BM convection in [21].

The present paper is organized as follows: In the next section, we give an overview on the hydrodynamic equations of motion for a fluid undergoing BM convection. We make the assumption of an infinite Prandtl number (high viscosity) and of a flat upper surface. The linearized problem yields the critical line in 2D space of control parameters where convection sets in. In the third part we calculate weakly nonlinear solutions, applying the formalism of amplitude equations. The stability of the two typically encountered basic patterns, namely, rolls and hexagons, is discussed with respect to their wavelength and the distance from threshold. Since there exists very little experimental material for BM convection that can be evaluated quantitatively, we perform in the fourth part direct numerical solutions of the 3D Navier-Stokes equations. Finally we present a two-dimensional model based on generalizations of earlier models that may reproduce the main features of pattern formation near the threshold of convection. Numerical solutions of this model are discussed.

II. THE BASIC EQUATIONS GOVERNING BM CONVECTION

A fluid with density ρ, viscosity η, and thermal conductivity κ is described by the velocity field $\mathbf{v}(\mathbf{r},t)$, the temperature field $T(\mathbf{r},t)$, the pressure $p(\mathbf{r},t)$, as well as a state equation for the density. The conservation laws for an incompressible fluid under the influence of an externally applied gravitational acceleration g read [6] as

$$\rho(\mathbf{r},t)\{\partial_t \mathbf{v}(\mathbf{r},t)+\mathbf{v}(\mathbf{r},t)\cdot\nabla\mathbf{v}(\mathbf{r},t)\}$$

$$=\rho(\mathbf{r},t)g\mathbf{z}_0-\nabla p(\mathbf{r},t)+\eta\Delta\mathbf{v}(\mathbf{r},t) ,$$

$$\nabla\cdot\mathbf{v}(\mathbf{r},t)=0 , \qquad (1)$$

$$\partial_t T(\mathbf{r},t)+\mathbf{v}(\mathbf{r},t)\cdot\nabla T(\mathbf{r},t)=\kappa\Delta T(\mathbf{r},t) ,$$

where $\mathbf{z}_0$ is the unit vector in vertical direction. In the Boussinesq approximation the variation of the density ρ is neglected except for the external force term, where it results in buoyancy effects. In this term a linear variation of density with the temperature is assumed:

$$\rho(T)=\rho_0\{1-\alpha[T(\mathbf{r},t)-T_0]\} , \qquad (2)$$

where T_0 is the temperature at the bottom plate and the thermal expansion coefficient is denoted by α.

For the general representation of the divergence-free velocity field we make the usual decomposition into a toroidal and a poloidal part, represented by two scalar fields:

$$\mathbf{v}(\mathbf{r},t)=\nabla\times\{\phi(\mathbf{r},t)\mathbf{z}_0\}+\nabla\times\nabla\times\{\psi(\mathbf{r},t)\mathbf{z}_0\} , \qquad (3)$$

where $\mathbf{z}_0$ is the unit vector in vertical direction. Introducing the variation $\Theta(\mathbf{r},t)$ of the temperature from the basic linear temperature profile and eliminating the pressure by forming the curl and twice the curl of the Navier-Stokes equations one arrives at the following set of evolution equations:

$$\left\{\Delta-\frac{1}{\mathrm{Pr}}\partial_t\right\}\Delta\Delta_2\psi(\mathbf{r},t)=R\,\Delta_2\Theta(\mathbf{r},t)-\frac{1}{\mathrm{Pr}}\{\nabla\times\nabla\times[\mathbf{v}(\mathbf{r},t)\cdot\nabla\mathbf{v}(\mathbf{r},t)]\}_z ,$$

$$\left\{\Delta-\frac{1}{\mathrm{Pr}}\partial_t\right\}\Delta_2\phi(\mathbf{r},t)=-\frac{1}{\mathrm{Pr}}\{\nabla\times[\mathbf{v}(\mathbf{r},t)\cdot\nabla\mathbf{v}(\mathbf{r},t)]\}_z , \qquad (4)$$

$$\{\Delta-\partial_t\}\Theta(\mathbf{r},t)=\Delta_2\psi(\mathbf{r},t)+\mathbf{v}(\mathbf{r},t)\cdot\nabla\Theta(\mathbf{r},t) ,$$

with the Prandtl number $\mathrm{Pr}=\eta/\rho_0\kappa$ and the horizontal Laplacian $\Delta_2=\partial_{xx}+\partial_{yy}$. Time and length are scaled by the vertical diffusion time κ/d^2 and the layer depth d, respectively, and all quantities are dimensionless. The first control parameter, R, the Rayleigh number, is given by

$$R=-\frac{\rho_0 g\alpha\beta d^4}{\kappa\eta} . \qquad (5)$$

R is proportional to the (negative) temperature gradient β. Assuming vanishing velocity components on the closed boundaries (rigid boundary conditions), (3) leads to

$$\phi(\mathbf{r},t)=\psi(\mathbf{r},t)=\partial_n\psi(\mathbf{r},t)=0 \qquad (6)$$

for $\mathbf{r}$ on the bottom and on the vertical walls and $\mathbf{n}$ perpendicular. On the lateral walls, we have, in addition,

$$\partial_n \phi(\mathbf{r}, t) = 0 \ , \quad \Delta_2 \psi(\mathbf{r}, t) = 0 \ . \tag{7}$$

General boundary conditions (BC) for the temperature field can be expressed in the form

$$\partial_z \Theta(\mathbf{r}, t) = \begin{cases} \mathrm{Bi}_0 \Theta(\mathbf{r}, t) & \text{for } z = 0 \ , \\ -\mathrm{Bi}_1 \Theta(\mathbf{r}, t) & \text{for } z = 1 \ , \end{cases} \tag{8}$$

where Bi is another dimensionless parameter, the so-called Biot number, standing for the ratio of the thermal conductivity of the corresponding wall and to that of the fluid. A perfectly conducting boundary corresponds to Bi $\to \infty$, a poorly heat conducting boundary to Bi $\ll 1$. In the following we assume that on the bottom of the layer $\mathrm{Bi}_0 \to \infty$, and, since air is a poor conductor compared to the commonly used fluids oil or water, on the upper surface $\mathrm{Bi}_1 = 0.1$. The last condition on the upper surface links the velocity field to the temperature (see, e.g., [8,9]). In terms of the variables Θ, ψ, and ϕ they read as

$$\partial_z \phi(\mathbf{r}, t) = 0 \ , \quad \psi(\mathbf{r}, t) = 0 \ , \quad \partial_z^2 \psi(\mathbf{r}, t) = -M \Theta(\mathbf{r}, t) \tag{9}$$

at $z = 1$. Here occurs the second control parameter of the system, the Marangoni number M:

$$M = \frac{\gamma \beta d^2}{\rho \nu \kappa} \ , \tag{10}$$

where the (negative) coefficient γ describes the linear dependence of the surface tension on the temperature along the surface [7,8]. If the temperature gradient β is increased, the ratio R/M remains constant. Therefore, the system can only move on lines that go to the origin of parameter space. From the two definitions (10) and (5) it is obvious that the ratio R/M of the two instability mechanisms and therefore the slope φ of these lines can be changed in the experiment by changing the depth of the fluid layer (see Fig. 2). In thin fluid layers, surface tension is the driving mechanism, in very thick (experimentally not accessible) layers, buoyancy forces are alone responsible for the formation of fluid patterns. In the following, that line will be called the "physical line."
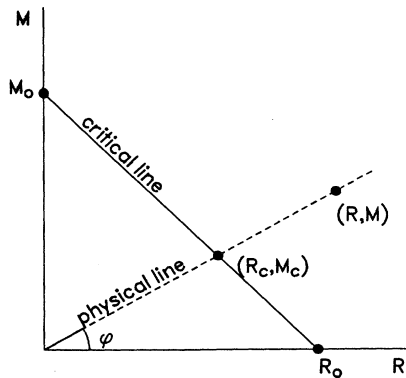
The onset of convection is marked by the critical line

FIG. 2. Two-dimensional space of control parameters. If the temperature gradient is increased, the system moves to the right on the physical line (dotted). On the right-hand side of the critical line, the motionless state gets unstable and pattern formation sets in. The slope $\tan(\varphi)$ of the physical line is proportional to the inverse of the height of the fluid layer.

(codimension one) [22]. From Fig. 2, we define the distance from threshold as

$$\epsilon = \frac{R - R_c}{R_c} = \frac{M - M_c}{M_c} \ .$$

In the following, we restrict our treatment to the case of a fluid with a large Prandtl number. This is a very good approximation for fluids such as water or oil, where Pr is clearly larger than 1. Then, the second equation of (4) reads as

$$\Delta \Delta_2 \phi(\mathbf{r}, t) = 0 \tag{11}$$

and, together with (6,7)

$$\phi(\mathbf{r}, t) = 0 \tag{12}$$

in the whole layer [23]. We are left with only two dependent variables, ψ and θ.

III. PATTERN FORMATION ABOVE THRESHOLD OF CONVECTION

In this section, we wish to describe pattern formation in the weakly nonlinear regime, i.e., in the vicinity of the critical line in the R-M plane. We therefore project the nonlinear solutions of the basic equations onto a certain number of Galerkin modes, namely, the eigenfunctions of the linearized system to Eq. (4) [24] and obtain a large system of coupled ordinary differential equations for their amplitudes. The slaving principle [16,24] then allows for a drastic reduction of dependent variables in mode space. After elimination of the enslaved (linearly damped) modes, we are left with a small system of equations that may be studied in detail, namely, the amplitude equations (AE). Using two particular solutions of the AE, rolls and hexagons, we compute stability boundaries depending on the wavelength of these patterns and the distance from threshold.

A. Amplitude equations

A general nonlinear solution of Eqs. (4) may be expressed by

$$\begin{bmatrix} \psi(\mathbf{r}, t) \\ \Theta(\mathbf{r}, t) \end{bmatrix} = \sum_l \int_{-\infty}^{\infty} d^2 k \, \xi_l(\mathbf{k}, t) \begin{bmatrix} f_l(k^2, z) \\ g_l(k^2, z) \end{bmatrix} e^{-i\mathbf{k} \cdot \mathbf{x}} \tag{13}$$

and

$$\xi_l(\mathbf{k}, t) = \xi_l^*(-\mathbf{k}, t) \ ,$$

where f and g are eigenfunctions of the linearized eigenvalue problem to (4) after performing the usual normal-model analysis [8,22]:

$$\begin{aligned} (d_z^2 - k^2)^2 f_l - R g_l &= 0 \ , \\ [d_z^2 - k^2 - \lambda_l(k^2)] g_l + k^2 f_l &= 0 \ , \end{aligned} \tag{14}$$

and l labels the different eigenfunctions. The functions f and g are calculated numerically by a finite difference method in vertical direction where the BC (8) and (9) can be implemented.

Inserting (13) into (4) yields, after multiplication with the adjoint function $g_l^+ \exp(i\mathbf{k} \cdot \mathbf{x})$ and integration over the spatial coordinates, the system

$$\partial_t \xi_l(\mathbf{k},t) = \lambda_l(k^2)\xi_l(\mathbf{k},t) - \sum_{l',l''}\int_{-\infty}^{\infty} d^2k' d^2k'' c_{l'l''}(\mathbf{k}\mathbf{k}'\mathbf{k}'')\xi_{l'}(\mathbf{k}',t)\xi_{l''}(\mathbf{k}'',t)\delta(\mathbf{k}-\mathbf{k}'-\mathbf{k}'') , \tag{15}$$

where the coefficients c are matrix elements that we compute directly from the basic equations for any given set of control parameters:

$$c_{l'l''}(\mathbf{k}\mathbf{k}'\mathbf{k}'') \equiv k'^2 \int_0^1 dz\, g_l^+(k^2,z)f_{l'}(k'^2,z)\partial_z g_{l''}(k''^2,z) - (\mathbf{k}',\mathbf{k}'')\int_0^1 dz\, g_l^+(k^2,z)g_{l'}(k'^2,z)\partial_z f_{l''}(k''^2,z) , \tag{16}$$

where $(\mathbf{k},\mathbf{k}')$ denotes the scalar product of $\mathbf{k}$ and $\mathbf{k}'$.

Here we are still at the same level of complexity; the infinitely many degrees of freedom intrinsic in the basic partial differential equations are expressed by an infinite number of mode amplitudes $\xi_l(\mathbf{k},t)$. To eliminate the fast modes by the linearly growing ones, we divide the eigenmodes into two groups [16,24,25]:

$$\lambda_l \rightarrow \begin{cases} \lambda_u(k) \approx 0 , \implies \xi_u(\mathbf{k},t) , & |\mathbf{k}| \approx k_c , \quad u \equiv l = 1 , \\ \lambda_s \ll 0 , \implies \xi_s(\mathbf{k},t) , & s \equiv l > 1 , \text{or } s \equiv l = 1 \text{ but } |\mathbf{k}| \neq k_c . \end{cases}$$

In the following we may therefore substitute the index l by u (unstable) or s (stable), depending on the values of l and $|\mathbf{k}|$. Now we express the amplitudes of the enslaved modes invoking an adiabatic elimination (k_c denotes the wave vector that maximizes λ_u). In this case, the dynamics of the enslaved modes is neglected, they follow instantaneously to the order parameters. The remaining equations for the order parameters ξ_u, the amplitude equations, read (here and in the following we suppress the index "u" at ξ and λ) as

$$\partial_t \xi(\mathbf{k},t) = \lambda(k)\xi(\mathbf{k},t) + \int d\mathbf{k}' d\mathbf{k}'' A(\mathbf{k},\mathbf{k}',\mathbf{k}'')\xi(\mathbf{k}',t)\xi(\mathbf{k}'',t)\delta(\mathbf{k}-\mathbf{k}'-\mathbf{k}'')$$
$$+ \int d\mathbf{k}' d\mathbf{k}'' d\mathbf{k}''' B(\mathbf{k},\mathbf{k}',\mathbf{k}'',\mathbf{k}''')\xi(\mathbf{k}',t)\xi(\mathbf{k}'',t)\xi(\mathbf{k}''',t)\delta(\mathbf{k}-\mathbf{k}'-\mathbf{k}''-\mathbf{k}''') , \tag{17}$$

where $|\mathbf{k}|, |\mathbf{k}'|, |\mathbf{k}''|, |\mathbf{k}'''| \approx |\mathbf{k}_c|$. If the system is isotropic in real space, the linear part of the AE may only depend on k^2, i.e., the unstable modes lie on a ring in Fourier space with radius k_c [17]. The Landau coefficients A and B in (17) are directly related to the matrix elements (16):

$$A(\mathbf{k},\mathbf{k}',\mathbf{k}'') = -c_{uuu}(\mathbf{k},\mathbf{k}',\mathbf{k}'') ,$$

$$B(\mathbf{k},\mathbf{k}',\mathbf{k}'',\mathbf{k}''') = \sum_s \frac{1}{\lambda_s(\mathbf{k}''+\mathbf{k}''')}c_{suu}(\mathbf{k}''+\mathbf{k}''',\mathbf{k}',\mathbf{k}'')[c_{uus}(\mathbf{k},\mathbf{k}',\mathbf{k}''+\mathbf{k}''')+c_{usu}(\mathbf{k},\mathbf{k}''+\mathbf{k}''',\mathbf{k}')] ,$$

where the indices u and s are defined above.

B. Two stationary solutions—Secondary instabilities

Now we discuss the stability of two particular time-independent solutions of Eqs. (17). One corresponds to parallel rolls with wave vector k_R, having the amplitudes

$$\xi(\mathbf{k}) = \begin{cases} \xi_R(k_R) , & \mathbf{k} = \pm \mathbf{k}_R , \\ 0 , & \text{otherwise} , \end{cases} \tag{18}$$

where

$$B_R(k_R)\xi_R^2(k_R) + \lambda(k_R) = 0$$

with

$$B_R(\mathbf{k}) \equiv B(\mathbf{k},\mathbf{k},\mathbf{k},-\mathbf{k}) + B(\mathbf{k},\mathbf{k},-\mathbf{k},\mathbf{k}) + B(\mathbf{k},-\mathbf{k},\mathbf{k},\mathbf{k}) .$$

The quadratic term A of (17) does not contribute to the roll amplitude since rolls may only couple to odd powers of the order parameter. The other stationary solution describes perfect hexagons with side length $4\pi/3k_H$ and is formed by the superposition of six plane waves:

$$\xi(\mathbf{k}) = \begin{cases} \xi_H(k_H) , & \mathbf{k}_c = \mathbf{k}_i , \quad i = 1,\dots,6 , \\ 0 , & \text{otherwise} , \end{cases} \tag{19}$$

and

$$\mathbf{k}_1 - \mathbf{k}_2 + \mathbf{k}_3 = 0 , \quad \mathbf{k}_{i+3} = -\mathbf{k}_i , \quad |\mathbf{k}_i| = k_H .$$

The index i labels the six different directions in 2D k space, see Fig. 3. The amplitude ξ_H is thereby defined as the larger root of

$$B_H(k_H)\xi_H^2 + A_H(k_H)\xi_H + \lambda(k_H) = 0 ,$$

with

$$A_H(k_H) \equiv A(\mathbf{k}_1,\mathbf{k}_2,-\mathbf{k}_3) + A(\mathbf{k}_1,-\mathbf{k}_3,\mathbf{k}_2) ,$$

$$B_H(k_H) \equiv \sum_{i=1}^{6} [B(\mathbf{k}_1,\mathbf{k}_1,\mathbf{k}_i,-\mathbf{k}_i) + B(\mathbf{k}_1,\mathbf{k}_i,\mathbf{k}_1,-\mathbf{k}_i)$$
$$+ B(\mathbf{k}_1,\mathbf{k}_i,-\mathbf{k}_i,\mathbf{k}_1)] .$$

We now examine the ranges of stability for the two above calculated solutions of rolls and hexagons in the k-ϵ plane. Therefore we consider infinitesimal disturbances u_j that may slowly vary in space with the small wave vector $\delta\mathbf{k}$:

$$\xi(\mathbf{k}) = \xi^0(\mathbf{k}_j) + u_j(\mathbf{k}_j + \delta\mathbf{k})e^{\sigma t} \tag{20}$$

with $\xi^0 = \xi_R, \xi_H$, respectively.

Inserting (20) into (17) and linearizing with respect to u_j gives the linear 6×6 eigenvalue problem [26]:
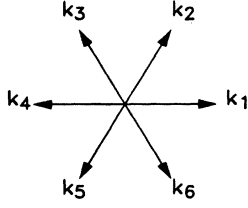
$$[\underline{M} - \sigma]\mathbf{u} = 0 , \tag{21}$$

FIG. 3. Arrangement of the six wave vectors forming regular hexagons.

FIG. 4. Basic hexagonal pattern (solid) and a pattern caused by phase instability (dashed) with δk parallel (left), δk perpendicular (right) to one of the six wave vectors.

where the matrix $\underline{M}$ depends on control parameters as well as on k and δk.

The solution of (21) for spatially homogeneous perturbations ($\delta k = 0$) may be obtained analytically. For hexagons, it yields the eigenvalues

$$\sigma_{1,2} = 0 , \quad \sigma_3 = -3A_H\xi_H < 0 ,$$

$$\sigma_{4,5} = \lambda(k_H) + 3B_R\xi_H^2 - A_H\xi_H ,$$

$$\sigma_6 = -2\lambda(k_H) - A_H\xi_H < 0 .$$

Here we may distinguish naturally between phase and amplitude instabilities: The first two eigenvalues are always zero, the eigenvalue of the general case $\delta k \neq 0$ will depend in lowest order on $(\delta k)^2$:

$$\sigma_{1,2} = \sigma_{1,2}^{(2)}(\delta k)^2 + O((\delta k)^4) .$$

For $\sigma^{(2)} > 0$, a pattern with a slightly different wave vector (sideband instability) from k_H can grow. The lines

$$\sigma^{(2)}(\epsilon, k_H) = 0$$

denote the phase stability boundaries in the ϵ-k plane of hexagons with side length $4\pi/3k_H$ [27]. In contrast to the case of rolls, the phase stability domain of hexagons is bounded also from above. A more detailed analysis of $\sigma^{(2)}$ shows that there exists no dependence of the phase-stability boundaries on the direction of δk with respect to the primary hexagons (see also [26]). This can be qualitatively understood by the fact that a hexagonal lattice has a sixfold rotational symmetry, in contrast to rolls, where the two domains bound by transversal (zigzag) and longitudinal (Eckhaus) instability are completely different. Figure 4 shows the linearly growing patterns for the two cases $\delta k \| k_1$ and $\delta k \perp k_1$.

The second group of eigenvalues $\sigma_{4,5,6}$ belongs to amplitude instabilities. The hexagons can become unstable to a spatially uniform disturbance with $\delta k = 0$. The line

$$\sigma_{4,5}(\epsilon, k_H) = 0$$

denotes the stability boundary with respect to the transition from hexagons to rolls. Figure 5(a) shows these two stability domains for a simplified model where only the liner part of (17) depend on k, i.e., all Landau coefficients in (17) are assumed to be constant.

Applying the same formalism on the linearization with respect to rolls, the 6×6 system (21) separates into three 2×2 systems. Two of them are equal and define the amplitude instabilities, here the transition rolls to hexagons,
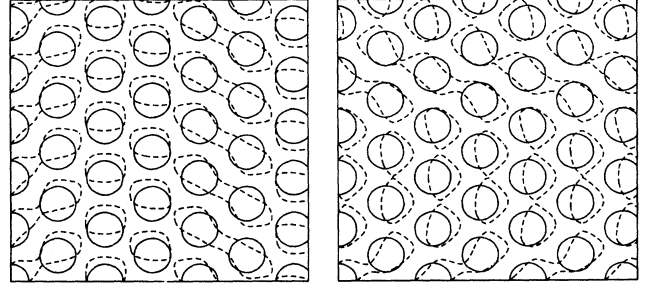
as a lower bound of ϵ. The remaining 2×2 system contains the phase instabilities, namely, the zigzag instability for $\delta k \perp k_R$ and the Eckhaus instability for $\delta k \| k_R$. The phase instabilities are not affected by the quadratic Landau coefficient A.

To be complete, we computed another important amplitude instability that confines the stability region for rolls. It is the cross-roll instability [18] and describes the growth of rolls with wave number close to the critical one but perpendicular to the primary roll pattern.

The cross-roll, Eckhaus, zigzag, and hexagon instabilities are sketched in Fig. 5(b), again for the approximation of constant Landau coefficients.

We note that the inclusion of phase instabilities shrinks the domain of stable hexagons as well as the size of the hysteric region considerably [Fig. 5(c)]. In contrast to rolls, the stability domain of hexagons is also bounded from above. This is in good agreement with experimental results of the stability of hexagonal convection cells in a non-Boussinesq fluid where the viscosity is strongly temperature dependent [28].

C. Some results for BM convection for various parameter values

Now we wish to present numerical computations of stability domains of rolls and hexagons when we also include the dependence of the Landau coefficients on wave vector k. We calculated all coefficients by solving the linearized problem by a finite difference method for certain values of the slope of the "physical line," as defined in Sec. II. Figures 6(a)–6(d) show the results. Due to the dependence of the cubic coupling on the wave vector, the stability lines of the transitions roll-hexagon and vice versa are inclined to the left. For small values of k, rolls are preferred since the value of the cubic cross-coupling term increases. The lines that denote the phase instability of hexagons are also inclined, but to the right-hand side. This is due to the shift of k_c, the wave vector that maximizes the linear part of (17), to larger values with increasing ϵ. For vanishing Marangoni number, i.e., for fully-buoyancy-driven convection, the situation resembles that one found in earlier calculations for convection between two closed surfaces [18]. The only stable patterns are rolls, their wavelength is limited by the zigzag instability
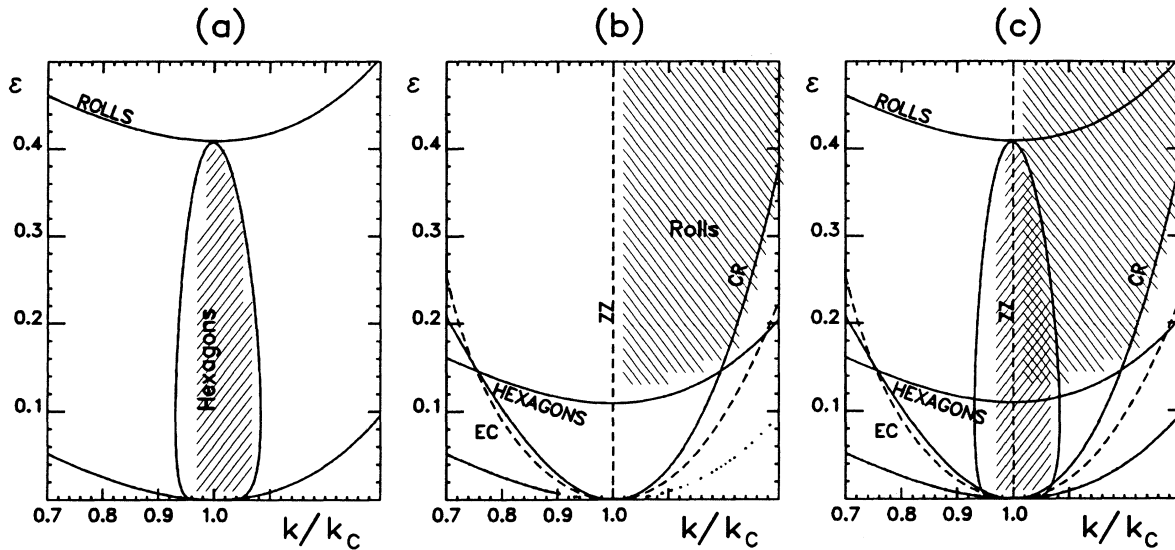
FIG. 5. Stability diagram for the case of constant Landau coefficients; (a) stable hexagons in the shaded area, restricted laterally by phase instabilities and vertically by transition to rolls (top) and transition to conduction (bottom), (b) stable rolls in the shaded area, confined by transition to hexagons, cross-roll (CR), and zigzag (ZZ) instability. EC denotes the longitudinal Eckhaus phase instability. (c) Hysteresis is found in the cross-hatched area in a relatively small region.
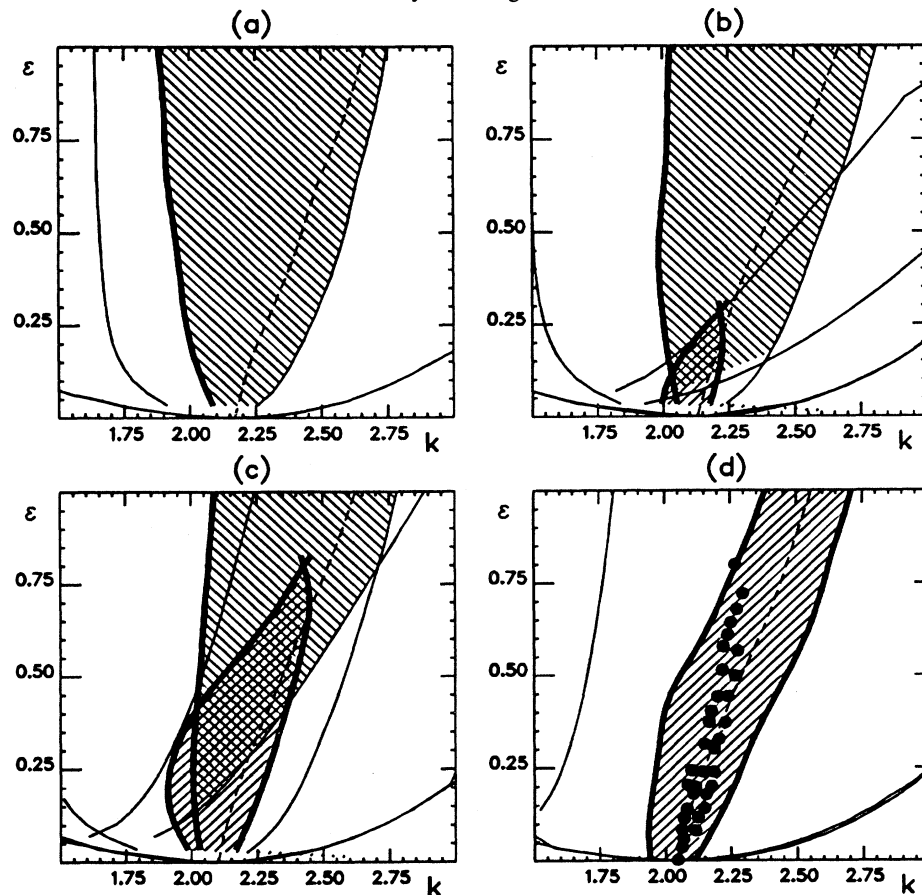

FIG. 6. Stability diagrams for Landau coefficients computed directly for BM convection for different angles φ of the physical line. Solid lines: amplitude instabilities (hexagon rolls and cross rolls); bold lines: phase instabilities; dotted lines: k_{max}, wave vector that maximizes the linear growth rate. (a) $\varphi=0$, no stable hexagons, rolls are limited by zigzag and cross-roll instability (down-hatched). (b) $\varphi=10°$, hexagons are stable in the small bubble (up-hatched) around k_c. (c) $\varphi=20°$, large area of stable hexagons, confined by phase instabilities. (d) $\varphi=70°$, no stable rolls possible, hexagons are stable in a small band around k_{max}. Black dots mark experimental data obtained from [19]. k in dimensionless units of Eqs. (4).

for large values and the cross-roll instability for small values [Fig. 6(a)]. If surface-tension effects are included but convection is still mainly buoyancy driven, the stability range for hexagons appears with a small bubble located around $k = k_c$ and $\epsilon = 0$ [Fig. 6(b)]. In experiments done for these parameter values, one should observe rolls even near threshold. Since it is difficult to find a liquid that has a low enough dependence of surface tension on temperature, all experiments in BM convection until now are done for the surface-driven case, i.e., for a much larger Marangoni number, corresponding to a situation shown in Fig. 6(d) [11,19,29,30]. But also here, the phase instabilities restrict the stability region for hexagons drastically to a narrow band around k_c and should therefore select the wavelength of the stabilized patterns in a more or less sharp region. Rolls cannot be stable, even at larger distance to threshold. In Fig. 6(d) we inserted experimental results on wavelength selection in BM convection extracted from the recent work of Koschmieder and Switzer [19]. The experimentally determined wavelengths lay all within our computed region of stability and confirm our calculations based on amplitude equations well, even up to 75% above threshold.

IV. NUMERICAL RESULTS OF 3D BASIC EQUATIONS FOR BM CONVECTION

Since there are only few experimental data on BM convection, we wish to present numerical results coming from a direct integration of the basic equations (4) for an infinite Prandtl number. After introducing the numerical method followed by a short discussion on numerical stability as well as numerical accuracy, we present several time series where the different instability mechanisms discussed in the previous section can be seen clearly.

A. Numerical method

We treat Eq. (4) with $\phi = 0$ in three spatial dimensions under periodic BC in horizontal directions. To perform the time integration, we use a semi-implicit one-step-forward scheme, where the linear part of (4) is treated implicitly, the nonlinear one explicitly:

$$\Delta^2 \psi(\mathbf{r}, t+\delta t) - R\Theta(\mathbf{r}, t+\delta t) = 0 ,$$

$$\left[\frac{1}{\delta t} - \Delta \right] \Theta(\mathbf{r}, t+\delta t) + \Delta_2 \psi(\mathbf{r}, t+\delta t) \qquad (22)$$

$$= \frac{\Theta(\mathbf{r}, t)}{\delta t} - \mathbf{v}(\mathbf{r}, t) \cdot \nabla \Theta(\mathbf{r}, t) ,$$

with δt being the time step. To invert the right-hand side of (22), we apply a fast Fourier transform (FFT) in the horizontal coordinates $\mathbf{x}$. To calculate the derivatives with respect to the vertical direction z, we use a finite difference method. Equations (22) take the discretized form in each layer i:

$$[\delta_{ij} k^4 - 2k^2 D_{ij}^{(2)} + D_{ij}^{(4)}]\psi_j(\mathbf{k}, t+\delta t) - R\Theta_i(\mathbf{k}, t+\delta t) = 0 , \qquad (23)$$

$$\left[\delta_{ij} \left[\frac{1}{\delta t} + k^2 \right] - D_{ij}^{(2)} \right] \Theta_j(\mathbf{k}, t+\delta t) - k^2 \psi_i(\mathbf{k}, t+\delta t)$$

$$= F_i(\mathbf{k}, t) ,$$

where one has to sum up over j on the right-hand side and the indices i, j denote the N meshpoints in the z direction, δ_{ij} the Kronecker symbol. $D_{ij}^{(n)}$ stands for the differential matrix of the nth derivative (see, e.g., [31]). The BC in the vertical direction are incorporated in $D_{ij}^{(n)}$, $D_{ij}^{(4)}$ depends on the Marangoni number, $D_{ij}^{(2)}$ in the second equation on the Biot number. We used central differences on the order δz. F_i denotes the Fourier transform of the left-hand side of (22) in layer i. If we combine Θ_i and ψ_i to a $2N$-component vector $\mathbf{U}$ of the form

$$\mathbf{U} = (\Theta_1, \psi_1, \ldots, \Theta_N, \psi_N) ,$$

the task we are left with is the inversion of a band matrix $\underline{L}$ at each time step:

$$\underline{L} \mathbf{U}(\mathbf{k}, t+\delta t) = \mathbf{G}(\mathbf{k}, t) \qquad (24)$$

that can be performed effectively using standard routines (see, e.g., [32]). Here, $\mathbf{G}$ is introduced as

$$\mathbf{G} = (F_1, 0, F_2, 0, \ldots, F_N, 0) .$$

An inverse FFT of $\Theta_i(\mathbf{k}, t+\delta t)$ and $\psi_i(\mathbf{k}, t+\delta t)$ to real space completes one iteration step. To avoid convolution sums in Fourier space, the nonlinearities are calculated in real space using again a finite difference method with grid spacing Δx, Δz for their derivatives. Switching between real and Fourier space is also known as "pseudo-spectral method" (see, e.g., [33]).

B. Stability

We wish to show the relation between the size of $\delta t, \Delta x, \Delta z$, and numerical stability. To this end we have to linearize (22) around a stable solution and examine the temporal behavior of an arbitrary disturbance. For the sake of simplicity we restrict the calculation here to the two-dimensional case and to free-free BC in the vertical direction. Then a stationary solution of (4) consists of parallel rolls and reads, up to the order ϵ, as

$$\Theta_0(x, z) = \frac{4}{\pi} \left[\frac{\epsilon}{3} \right]^{1/2} \sin(\pi z)\cos k_c x + \frac{\epsilon}{\pi}\sin 2\pi z ,$$

$$\psi_0(x, z) = \frac{4}{\pi}\sqrt{3\epsilon}\sin(\pi z)\cos k_c x , \qquad (25)$$

with $k_c = \pi/\sqrt{2}$. Inserting (25) into (22) and linearizing with respect to small disturbances $\mathbf{u}(\mathbf{k}, t)$ added to (25), (24) yields a linear iteration rule for $\mathbf{u}$ in Fourier space:

$$\underline{L} \mathbf{u}(\mathbf{k}, t+\delta t) = \underline{N} \mathbf{u}(\mathbf{k}, t) \qquad (26)$$

with the matrix elements of $\underline{N}$ given as

$$N_{ij} = \frac{\delta G_i}{\delta U_j} \bigg|_{\Theta = \Theta_0, \psi = \psi_0} .$$

The condition for numerical stability is now that the spectral radius of the amplification matrix $\underline{Q}$,

$$\underline{Q} = \underline{L}^{-1}\underline{N} \ , \tag{27}$$

is less than 1. We evaluated the spectrum of (27) numerically for several step sizes Δz, Δx, and δt (Fig. 7). Up to rather large values of ϵ, we found the restriction

$$\delta t < \frac{C(\Delta x)}{\epsilon} \ ,$$

where C increases monotonically with Δx but is more or less independent of Δz. Some value for C and Δx are $C = 0.030$, $\Delta x = \lambda_c/4$, $C = 0.021$, $\Delta x = \lambda_c/6$, $C = 0.017$, $\Delta x = \lambda_c/8$, and $C = 0.013$, $\Delta x = \lambda_c/10$ with $\lambda_c = 2\pi/k_c$. Finally, we note that the restriction on the time step to ensure numerical stability is much weaker than that for a fully explicit scheme. This justifies the larger numerical effort of the semi-implicit method.

C. Accuracy

The single-step-forward method yields an accuracy of order δt in time [33]. The remaining relative truncation error $\mathscr{E}_{\mathrm{err}}$ is of order $(\delta t)^2$ and is determined near the above calculated fixed point by:

$$\mathscr{E}_{\mathrm{err}}(\delta t) = 2\max_i[\Lambda_i^2(\delta t/2) - \Lambda_i(\delta t)] \ , \tag{28}$$

where $\Lambda_i(\delta t)$ denote the eigenvalues of $\underline{Q}$ for given δt. Figure 8 shows values for the truncation error in percents for several values of ϵ as a function of the time step. Due to the increase of the spectral radius of $\underline{Q}$ when the product $\epsilon\,\delta t$ approaches the region where the numerical method gets unstable, the truncation error changes sign and increases strongly in magnitude. From Fig. 8, the relation

$$\mathscr{E}_{\mathrm{err}}(\delta t) \approx \mathrm{const} \times (\epsilon\delta t)^2$$

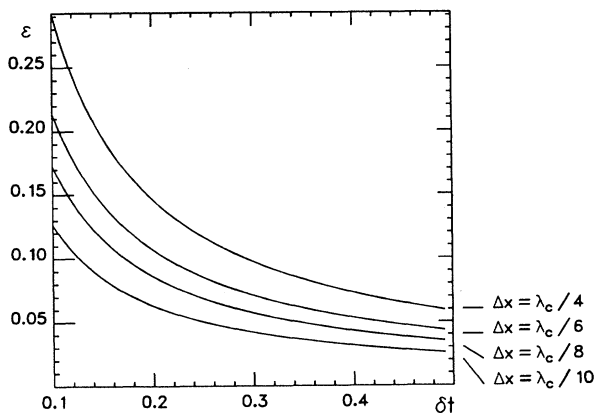with $\mathrm{const} \approx 75$ for small $\epsilon\,\delta t$ can be extracted.

FIG. 7. The numerical code for the 3D integration of Navier-Stokes and temperature equation is stable under the hyperboles that depend on δx but that are more or less independent of δz.
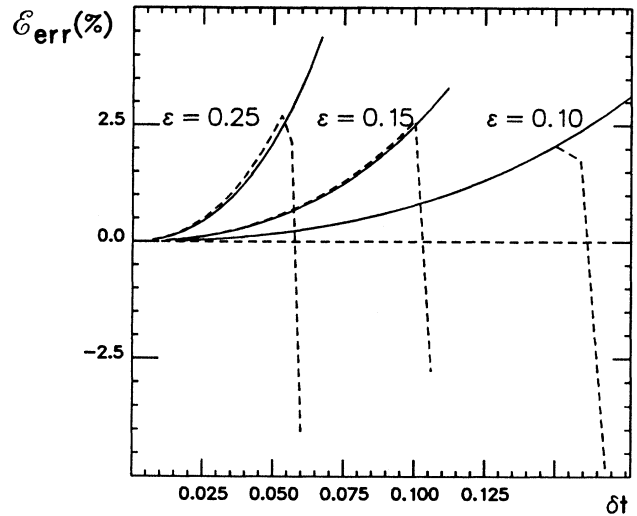
FIG. 8. Numerical error in percent of the two eigenmodes (solid and dashed) that belong to the two largest eigenvalues as a function of time step for several ϵ.

D. Results

The numerical code was implemented on a VAX station 4000-60 computer. The time series on which we report in this section were calculated on a mesh with $96 \times 72 \times 15$ points. This geometry allows a regular hexagonal pattern to fit within the periodic lateral BC. For this grid size, the method takes 14 s CPU time for one time iteration. To ensure sufficient accuracy as well as numerical stability, we choose always $\epsilon\,\delta t < 0.01$. To achieve a stationary solution, where the changes in the dependent variables from one time step to the following are less than the numerical round of error of the machine, we need about 10 000 iteration steps, resulting in about 40 h of CPU time for each run.

Evolution of random dot patterns. Starting with a randomly distributed temperature field, we performed two runs for both the extreme cases of purely buoyancy-driven convection $(\varphi = 0)$ and completely surface-driven convection $(\varphi = 90°)$. Figure 9 shows the formation of rolls as well as the motion and eventually the pairwise annihilation of defects until a regular roll structure is stabilized. This is in good agreement with computations of 2D equations (see also the next section) that model convection between rigid surfaces and periodic lateral BC [14].

On the other hand, surface-driven convection leads after rather short evolution time to the formation of small cells and finally to a stable hexagonal pattern (Fig. 10). The final solution shows still a large number of defects. The hexagon pattern is less flexible and penta-hepta defects cannot slide in the same way through the structure as roll defects. Since the time for spontaneous nucleation of hexagons out of the random initial condition is proportional to ϵ in contrast to the propagation speed of a hexagonal domain wall in lateral direction that is proportional to $\sqrt{\epsilon}$ [34], the number of defects increases with ϵ, because local regions of hexagons with

different orientations are formed at an early stage of evolution (see also the discussion for the formation of rolls in a 2D model, [35]). The increase of the number of defects with ϵ is also known from experiments [30]. This may also explain the very regular hexagonal structures often found in experiment if ϵ is driven extremely slowly through threshold [11,19].

Phase unstable rolls, leading to hexagons and vice versa. We wish to examine the development of a perfect pattern (parallel rolls or hexagons without dislocations) if its wave number lies outside the stable regions of the phase diagrams computed in Sec. III. To this end we start with a perfect pattern as the initial condition with the wave vector inside the stable region, usually with $|k| = k_c$. After nonlinear saturation and complete stabilization of this pattern we change the step size Δx of the horizontal coordinates. This has the same effect as changing the aspect ratio as well as the wavelength and enlarges or shrinks the whole structure. Then we trigger a possible instability by adding small random perturbations and examine their spatial evolution in the course of time.

We start with a relatively small M_c, corresponding to $\varphi = 20°$ and a perfect roll pattern having its wave vector in the zigzag unstable domain of Fig. 6(c). The zigzag instability indeed occurs rapidly and leads to an almost perfect hexagonal pattern (Fig. 11). The small asymmetry

FIG. 10. Same as Fig. 9, but for $\varphi = 90°$ where convection is purely surface driven. Different regions of hexagons are formed soon and give rise to a stable pattern showing some grain boundaries and lines of penta-hepta defects.
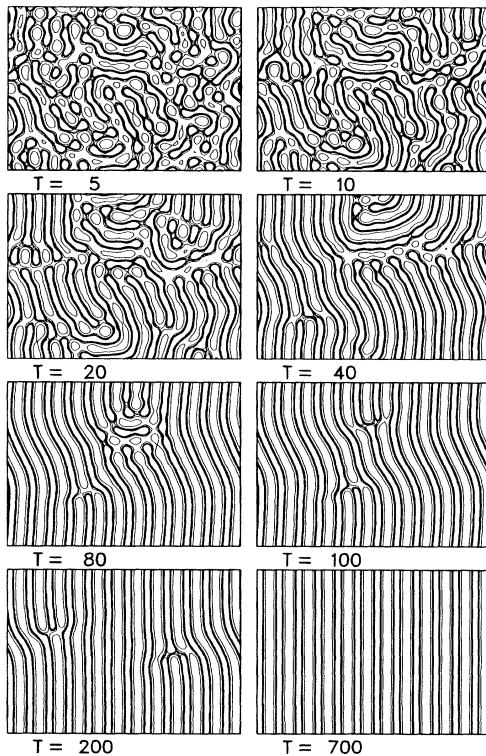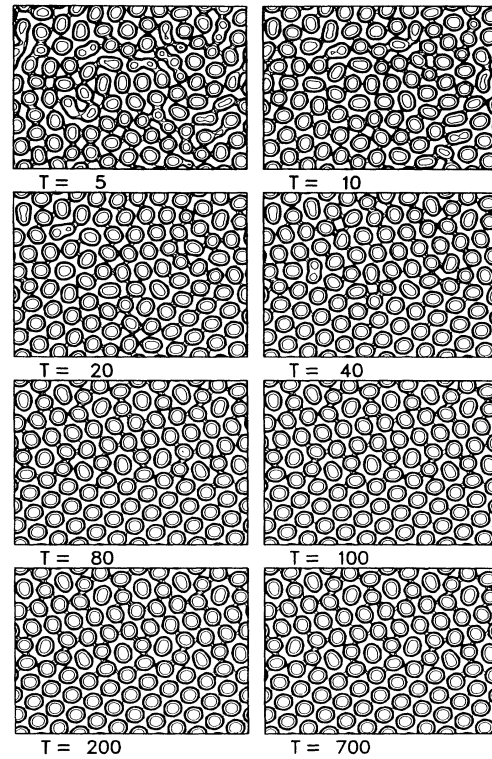

FIG. 9. Time series of a random dot initial pattern in the completely buoyancy-driven case. Shown is the temperature field as viewed from the top of the layer. Completely parallel rolls are formed eventually. For this and all the following series we fixed the control parameters to 25% above threshold. $\varphi = 0°$, aspect ratio $\Gamma_x = 34.7 = 12.0\lambda_c$, $\Gamma_y = 26.2 = 9.0\lambda_c$.
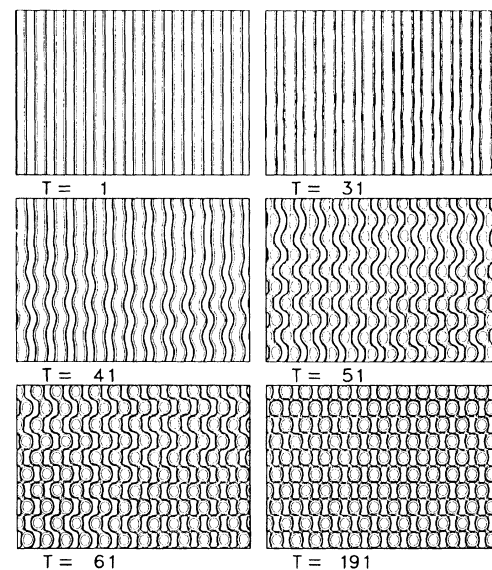

FIG. 11. Phase instability of rolls that lie outside the stable region in phase space. Clearly seen is the zigzag instability that leads eventually to an asymmetric hexagonal pattern, forced by the periodicity length of the lateral boundaries. $\varphi = 20°$, $\Gamma_x = 40.8 = 13.7\lambda_c$, $\Gamma_y = 30.6 = 10.3\lambda_c$.
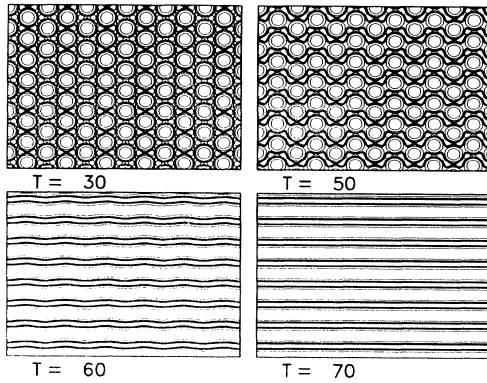
FIG. 12. Phase instability of hexagons with a wave number that is too large $(k=2.6)$. After a relatively short transient phase rolls within the stable wave number range $(k=2.25)$ are formed and completely stabilized. $\varphi=20°$, $\Gamma_x=29=9.7\lambda_c$, $\Gamma_y=21.8=7.3\lambda_c$.

there is caused by the fact that regular hexagons cannot match the periodic lateral BC exactly for this aspect ratio. Figure 12 shows the case, where a perfect hexagon pattern with the wave vector outside of the right boundary of the stable region of Fig. 6(c) evolves via a phase instability to a regular roll pattern.
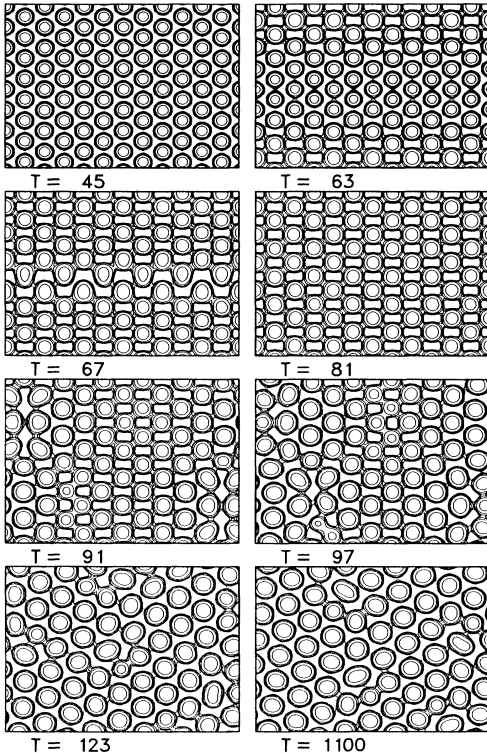

FIG. 13. Phase instability of hexagons with a wave number that is too large $(k=2.7)$, now in the surface-driven regime. Two temporally separated transient phases can be seen, caused by phase instabilities. The first goes to asymmetric hexagons by a kind of cell fusion [28] that change again to an eventually stable hexagonal pattern with a large number of defects. $\varphi=70°$, $\Gamma_x=27.9=9.3\lambda_c$, $\Gamma_y=20.9=7.0\lambda_c$.

Phase instabilities for hexagons. Now we switch to large M_c, where convection is almost completely surface drive $(\varphi=70°)$ and no stable rolls can exist even far above threshold. We performed two runs at $\epsilon=0.25$, one with a wave vector too large (Fig. 13), the other one with a wave number too small (Fig. 14), according to the stability diagram Fig. 6(d). In both cases, hexagons within the stable region evolve after a relatively long time. Two different processes can be recognized in the early stages of Figs. 13 and 14. In Fig. 13, a fusion of hexagons takes place in the central stripe of the layer $(t=67)$. In Fig. 14 a pattern very similar to the so-called mosaic instability of [28] can be detected for $t=86$. Smaller hexagons, located at the places of the initial cells, are surrounded by six larger hexagons. This and also the mechanism of cell fusion was obtained experimentally in [28].

An experimentally accessible quantity is the Nusselt number. It measures the heat flux through the fluid layer and can be computed by [9]

$$\text{Nu}(t)=1-\langle\partial_z\Theta(\mathbf{r},t)|_{z=0}\rangle_{x,y} , \tag{29}$$

where $\langle\ \rangle_{x,y}$ denotes the average over the horizontal coordinates. Its temporal development shows the different stages of pattern formation. Nusselt numbers corresponding to the pattern series, Fig. 13, are presented in Fig. 15.
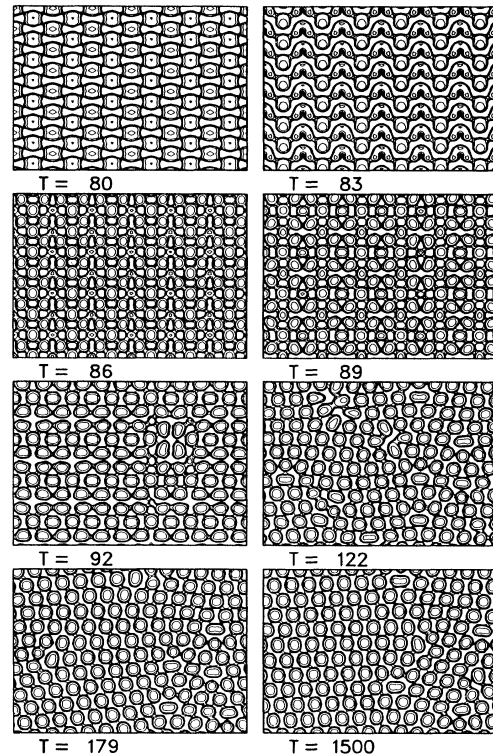
All the numerical runs performed above give an outline

FIG. 14. Phase instability of hexagons with a wave number that is small $(k=1.7)$, again in the surface-driven regime. The state at $t=86$ resembles the mosaic instability in [28]. The pattern shown in the last frame is stable. $\varphi=70°$, $\Gamma_x=44.4=14.8\lambda_c$, $\Gamma_y=33.2=11.1\lambda_c$.
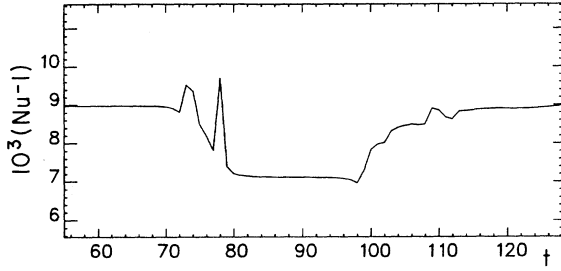
FIG. 15. Temporal behavior of the Nusselt number that belongs to the series shown in Fig. 13. The first transient (fusion) to asymmetric hexagons $(t \approx 75)$ leads to a lower value for Nu but the resulting pattern is again unstable against phase disturbances. The second transient $(t \approx 100)$ increases Nu again and leads to hexagons inside the stable regime in the k-ϵ plane.

of pattern formation in 3D convection under the influence of several phase and amplitude instabilities. They confirm well the phase diagrams obtained in the previous section based on amplitude equations, even up to a range of 25–50% above threshold.

V. A TWO-DIMENSIONAL MODEL EQUATION DESCRIBING BM CONVECTION NEAR THRESHOLD

After direct numerical treatment of the Navier-Stokes equation, which is still rather time consuming, we turn back to the approach considered in Sec. III. There we derived two-dimensional amplitude equations in Fourier space by projection onto eigenfunctions in the vertical direction and elimination of the linearly damped amplitudes.

A. The model

The decisive drawback of amplitude equations is the lack of a rotationally invariant formulation in 2D real space. This would require an infinite number of coupled equations of the form of Eq. (17) since there are infinitely many directions. A quite elegant method is the construction of a rapidly varying wave function that contains the whole spatial dependence of the order parameter [16]. Therefore, we sum up over all directions in real space according to

$$\Psi(\mathbf{x},t) = \int_0^{2\pi} d\beta \, \xi_\beta(\mathbf{x},t) e^{i k c(\beta) \cdot \mathbf{x}} , \qquad (30)$$

where $\xi_\beta(\mathbf{x},t)$ is the Fourier transform of $\xi(\mathbf{k}(\beta) - \mathbf{k}_c(\beta), t)$ and, since $|k| \approx |k_c|$, is slowly varying in real space. The angle β denotes the orientation of $\mathbf{k}$ in 2D Fourier space. Inserting (30) into (17) yields, after a Fourier transform to real space, a nonlocal nonlinear equation for Ψ (for details see [16]). The nonlinearities may be approximated by gradient expansion of the kernel. This leads to a local order parameter equation for the scalar function Ψ in form of a partial differential equation, the generalized Ginzburg-Landau equation that reads [17,36] as

$$\dot{\Psi}(\mathbf{x},t) = [\gamma_1 \epsilon - \gamma_2 (k_c^2 + \Delta_2)^2] \Psi(\mathbf{x},t) - a_1 [\nabla_2 \Psi(\mathbf{x},t)]^2$$

$$- a_2 \Psi(\mathbf{x},t) \Delta_2 \Psi(\mathbf{x},t)$$

$$- b_1 \Psi(\mathbf{x},t)[\Delta_2 \Psi(\mathbf{x},t)]^2 - b_2 \Psi(\mathbf{x},t) \Delta_2^2 \Psi^2(\mathbf{x},t) . \qquad (31)$$

The coefficients γ_i follow from a Taylor expansion of λ around k_c and R_c. The nonlinear coefficients a_i and b_i are calculated by comparing the mode coupling of (31) with that of (17), where a fitting to certain coupling angles between two plane waves is required. In particular, we require an exact coupling to modes with $k = 0$ and $k = 2k_c$. Table I shows some values for the coefficients computed by that method for different angles of the physical line.

The same procedure for the computation of secondary instabilities as described in Sec. III can be applied and yields qualitatively comparable results. In particular we find the transitions from rolls to hexagons and back, as well as stability boundaries of rolls and hexagons with respect to phase instabilities. We note that other approximations of the nonlocal expressions lead to other models, some of them were discussed in detail in previous works [5,14,15,17,37–39]. A simplified model showing the formation of hexagons in this context was derived first in [16] and treated numerically in [40].

Going back to (13) and (3), we may express the hydrodynamic variables $\mathbf{v}$ and Θ by the wave function Ψ. The relations read in lowest order of the 2D order parameter:

$$\mathbf{v}(\mathbf{r},t) = \nabla \times \nabla \times \{f_1(\Delta_2,z)\Psi(\mathbf{x},t)\mathbf{z}_0\} + O(\Psi^2) ,$$

$$\Theta(\mathbf{r},t) = g_1(\Delta_2,z)\Psi(\mathbf{x},t) + O(\Psi^2) . \qquad (32)$$

Due to its k^2 dependence, the eigenfunctions f_1, g_1 defined in (14) are now differential operators. Keeping in mind that the Fourier representation of Ψ is mainly excited on a ring with radius k_c, we may substitute the Laplacians in the eigenvectors by $-k_c^2$. Then the eigenvectors are simple functions of z again. In this approximation, the relations to the basic variables read as

$$\mathbf{v}(\mathbf{r},t) = \begin{vmatrix} d_z f_1(k_c^2,z)\partial_x \Psi(\mathbf{x},t) \\ d_z f_1(k_c^2,z)\partial_y \Psi(\mathbf{x},t) \\ -f_1(k_c^2,z)\Delta_2 \Psi(\mathbf{x},t) \end{vmatrix} + O(\Psi^2) ,$$

$$\Theta(\mathbf{r},t) = g_1(k_c^2,z)\Psi(\mathbf{x},t) + O(\Psi^2) . \qquad (33)$$

From these relations, we derive immediately boundary

TABLE I. Numerical values for the coefficients of the generalized Ginzburg-Landau model introduced in Sec. V. The values were computed for several angles φ of the physical line, compared Fig. 2.

φ	k_c	γ_1	γ_2	a_1	a_2	b_1	b_2
0°	2.17	7.5	0.085	2.2	1.1	−0.01	0.19
10°	2.14	7.2	0.084	2.6	1.1	−0.04	0.20
20°	2.11	6.9	0.082	3.1	1.1	−0.07	0.21
70°	2.05	6.3	0.078	3.8	0.3	−0.21	0.27
90°	2.03	6.2	0.073	4.6	0.2	−0.29	0.31

conditions for Ψ on the lateral walls. Assuming vanishing horizontal velocity and temperature field (poor thermal conductors), they are

$$\partial_n \Psi(\mathbf{x},t) = \Psi(\mathbf{x},t) = 0 \qquad (34)$$

for $\mathbf{x}$ on and $\mathbf{n}$ perpendicular to the lateral walls.

B. Results

The numerical effort of the treatment of 2D models as (31) is much lower than that of the 3D basic equations and the inclusion of rigid lateral BC (34) can be reached more easily. We use again a semi-implicit pseudo-spectral code, allowing for a large time step during periods of small changes in pattern formation. The method is described in more detail in [39]. We performed solutions for periodic BC and found very similar results to those obtained in Sec. IV that we do not want to repeat here in detail. Using rigid BC (34) and a circular lateral wall, we also computed solutions for a rather large aspect ratio, to show the role of sidewall forcing and defect motion. Here we wish to present only two time series resulting of the evolution of a random dot pattern for different parameters. Figure 16 shows the case for purely buoyancy-driven convection, $\varphi = 0°$. Rolls are formed showing dislocations and grain boundaries in the bulk for early stages of evolution. In contrast to periodic BC, the dislocations cannot move freely and cannot annihilate. After a very long transient phase a pattern of slightly

FIG. 17. Same as Fig. 16, but for the surface-driven case. Hexagons are created in an early stage of the evolution and form stable domain boundaries that separate regions with different orientation. $\varphi = 90°$, $\Gamma = 198 = 64\lambda_c$, $\epsilon = 0.06$.

bended rolls in the bulk is stable. The grain boundaries still present originate from the sidewall. Nevertheless the dynamics of pattern evolution tries to minimize the length of these grain boundaries. Figure 17 shows the opposite case, where convection is completely surface driven ($\varphi = 90°$). Hexagons are formed soon and are stable, showing defects. Stable grain boundaries separate regions where hexagons have different orientation. Again the number of defects increases with the distance from threshold ϵ.

VI. CONCLUSION AND OUTLOOK

We presented a detailed theoretical investigation of a relatively simple pattern-forming system far from equilibrium. We showed the restriction of stability for primary patterns of convection, such as rolls and hexagons, if spatially inhomogeneous disturbances are taken into account. This can be considered as an extension of "Busse's balloon," computed for parallel rolls in Rayleigh-Bénard convection [18]. For our analysis we made two important assumptions: the Prandtl number was assumed being infinite, this is surely a good approximation for all common fluids, where Pr is in the range of 10 or larger. However, for convection in gases under high pressure (Pr < 1), the toroidal velocity field can no longer be neglected and gives rise to another order parameter in the frame of amplitude or generalized Ginzburg-Landau equations. Recent experiments in gases can be found in [41], also including non-Boussinesq effects. First model calculations based on order-parameter equations as de-
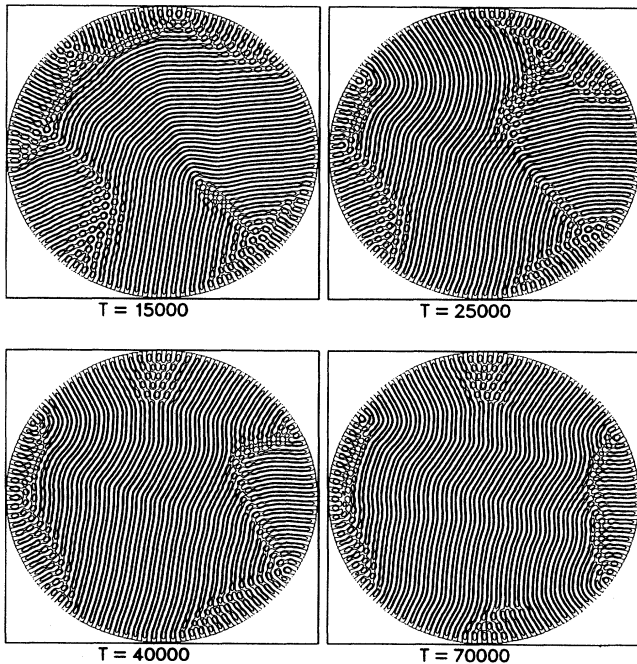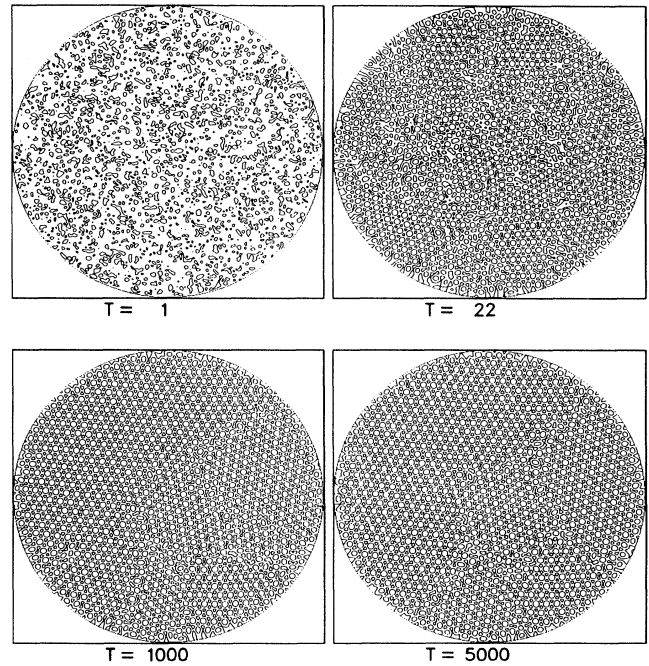

FIG. 16. Temporal evolution of an initial random dot pattern, found by integration of the order parameter equation (31) for rigid boundary conditions along a circular side wall. Due to the lower numerical effort, the aspect ratio can be chosen very large. Coefficients of the model equation were determined for the buoyancy driven case. $\varphi = 0°$, $\Gamma = 185 = 64\lambda_c$, $\epsilon = 0.075$.

scribed in Sec. V are published in [39]. The other assumption is that of a flat upper surface. In experiment, the free surface becomes slightly deflected above threshold. It could be interesting to see what the inclusion of these two effects would change qualitatively.

Another important purpose of this work was to show to what extent pattern formation in a certain nonequilibrium system can be modeled by a unified and simplified approach based on generalized Ginzburg-Landau equations. In the last part we saw that even quantitative features such as wave-length selection and creation and stability of dislocations can be compared directly with results found by integration of the hydrodynamic equations. Beneath their unifying character the great advantage of these models is a drastic simplification and therefore a considerable decrease of the numerical effort for their treatment. This allows one to consider pattern formation in very extended geometries under physical lateral boundary conditions and could be an important tool for the study of defect statistics and defect motion.

ACKNOWLEDGMENTS

[1] H. Bénard, Rev. Gen. Sci. Pur. Appl. 11, 1261 (1900).
[2] C. Normand, Y. Pomeau, and M. Verlarde, Rev. Mod. Phys. 49, 581 (1977).
[3] F. H. Busse, Rep. Prog. Phys. 41, 1931 (1978).
[4] R. P. Behringer, Rev. Mod. Phys. 57, 657 (1985).
[5] R. Friedrich, M. Bestehorn, and H. Haken, Int. J. Mod. Phys. B 4, 365 (1990).
[6] S. Chandrasekhar, Hydrodynamic and Hydromagnetic Stability (Clarendon, Oxford, 1961).
[7] R. A. Pearson, J. Fluid. Mech. 4, 489 (1958).
[8] C. Yih, Fluid Mechanics (McGraw-Hill, New York, 1969).
[9] J. K. Platten and J. C. Legros, Convection in Liquids (Springer-Verlag, Berlin, 1984).
[10] P. Manneville, Dissipative Structures and Weak Turbulence (Academic, New York, 1990).
[11] E. L. Koschmieder, Adv. Chem. Phys. 26, 177 (1974).
[12] A. C. Newell and J. A. Whitehead, J. Fluid. Mech. 38, 279 (1969); A. C. Newell, in Propagation in Systems Far from Equilibrium, edited by J. E. Wesfreid, H. R. Brand, P. Manneville, G. Albinet, and N. Boccara, Springer Series in Synergetics Vol. 41 (Springer, Berlin, 1988).
[13] L. A. Segel, J. Fluid Mech. 19, 203 (1969).
[14] J. Swift and P. C. Hohenberg, Phys. Rev. A 15, 319 (1977).
[15] H. S. Greenside and M. C. Cross, Phys. Rev. A 31, 2492 (1985).
[16] H. Haken, Advanced Synergetics, 2nd ed. (Springer, Berlin, 1987).
[17] M. Bestehorn and H. Haken, Phys. Rev. A 42, 7195 (1990).
[18] F. H. Busse, J. Math. Phys. 46, 149 (1967); in Hydrodynamic Instabilities and the Transition to Turbulence, edited by H. L. Swinney and J. P. Gollub (Springer, Berlin, 1981).
[19] E. L. Koschmieder and D. W. Switzer, J. Fluid Mech. 240, 533 (1992).
[20] F. H. Busse, J. Fluid. Mech. 30, 625 (1967).
[21] M. Bestehorn and C. Pérez-García, Europhys. Lett. 4, 1365 (1987).
[22] D. A. Nield, J. Fluid. Mech. 19, 341 (1964).
[23] This can be shown in general using Green's theorem after multiplication of (11) with ϕ and integration over the spatial coordinates.
[24] H. Haken, Synergetics. An Introduction, 3rd ed. (Springer, Berlin, 1983).
[25] H. Haken, Rep. Prog. Phys. 52, 515 (1989).
[26] B. Caroli, C. Caroli, and B. Roulet, J. Cryst. Growth 68, 677 (1984).
[27] This coincides with the change of sign of the diffusion coefficients of the phase equations for a perfect hexagonal lattice, as shown in a recent work by J. Lauzeral and D. Walgraef (unpublished).
[28] D. B. White, J. Fluid. Mech. 191, 247 (1988).
[29] J. Pantaloni, J. Bailleux, J. Salan, and M. G. Velarde, J. Non-Equil. Therm. 4, 405 (1979).
[30] P. Cerisier, C. Pérez-García, C. Jamond, and J. Pantaloni, Phys. Fluids. 30, 954 (1987).
[31] C. Hirsch, Numerical Computation of Internal and External Flows I, II (Wiley, Chichester, 1988).
[32] W. H. Press, B. P. Flannery, S. A. Teukolsky, and W. T. Vetterling, Numerical Recipes (Cambridge Univ. Press, New York, 1986).
[33] C. A. J. Fletcher, Computational Techniques for Fluid Dynamics (Springer, Berlin, 1989), Vol. I.
[34] D. G. Aronson and H. F. Weinberger, in Partial Differential Equations and Related Topics, edited by J. A. Goldstein, Lecture Notes in Mathematics Vol. 446 (Springer, New York, 1975).
[35] M. Bestehorn and H. Haken, Z. Phys. B 82, 305 (1991).
[36] M. Bestehorn, in Evolution of Dynamical Structures in Complex Systems, edited by R. Friedrich and A. Wunderlin (Springer, Berlin, 1992).
[37] V. L. Gertsberg and G. I. Sivashinsky, Prog. Theor. Phys. 66, 1219 (1981).
[38] J. Millán Rodriguez, C. Pérez-García, M. Bestehorn, M. Frantz, and R. Friedrich, Phys. Rev. A 46, 4729 (1992).
[39] M. Bestehorn, M. Fantz, R. Friedrich, and H. Haken, Phys. Lett. A 174, 48 (1993); M. Bestehorn, M. Fantz, R. Friedrich, H. Haken, and C. Pérez-García, Z. Phys. B 88, 93 (1992).
[40] M. Bestehorn and H. Haken, Phys. Lett. 99A, 265 (1983).
[41] E. Bodenschatz, J. R. de Bruyn, G. Ahlers, and D. S. Cannell, Phys. Rev. Lett. 67, 3078 (1991).